Preprint

M. Hlawatsch, P. Leube, W. Nowak, and D. Weiskopf,
"Flow Radar Glyphs — Static Visualization of Unsteady Flow with Uncertainty",
In *IEEE Transactions on Visualization and Computer Graphics* , in print,
vol. 17, no. 12, pp. xxx--xxx, Dec. 2011.

Flow Radar Glyphs — Static Visualization of Unsteady Flow with Uncertainty

Marcel Hlawatsch, Philipp Leube, Wolfgang Nowak, and Daniel Weiskopf, *Member, IEEE Computer Society*

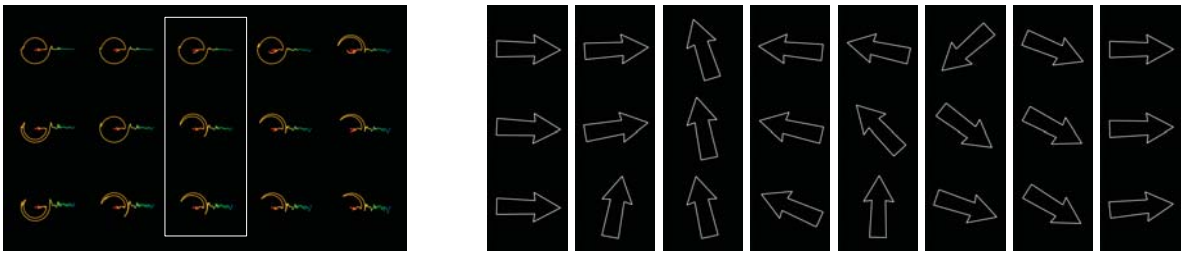

Fig. 1. Flow radar glyphs (left) in comparison to an animation of classic vector glyphs (right). The marked area (left image) is shown as a sequence of arrow glyphs (from left to right in the right image). The flow radar glyphs cover the full time range of the data set; the sequence of arrow glyphs covers only a smaller time range, colored yellow in the flow radar glyphs. The differences in spatiotemporal flow behavior can be detected fast and easily with flow radar glyphs. In this example, only the upper position exhibits a full rotation. With animated classic vector glyphs, the same task requires watching the animation multiple times. Even then it is hard with animated vector glyphs to analyze and compare the flow behavior over a large time range of the flow, e.g., to detect the stronger oscillations in the bottom region at the end of the time range.

Abstract—A new type of glyph is introduced to visualize unsteady flow with static images, allowing easier analysis of time-dependent phenomena compared to animated visualization. Adopting the visual metaphor of radar displays, this glyph represents flow directions by angles and time by radius in spherical coordinates. Dense seeding of flow radar glyphs on the flow domain naturally lends itself to multi-scale visualization: zoomed-out views show aggregated overviews, zooming-in enables detailed analysis of spatial and temporal characteristics. Uncertainty visualization is supported by extending the glyph to display possible ranges of flow directions. The paper focuses on 2D flow, but includes a discussion of 3D flow as well. Examples from CFD and the field of stochastic hydrogeology show that it is easy to discriminate regions of different spatiotemporal flow behavior and regions of different uncertainty variations in space and time. The examples also demonstrate that parameter studies can be analyzed because the glyph design facilitates comparative visualization. Finally, different variants of interactive GPU-accelerated implementations are discussed.

Index Terms—Visualization, glyph, uncertainty, unsteady flow.

1 Introduction

Many phenomena in science are time-dependent and can only be observed with appropriate visualization. An intuitive, common, and straightforward approach is to create a time-dependent visualization by generation and playback of a sequence of images. In many cases, however, this is not the best approach because it relies on human memory and puts heavy load on human visual cognition. Therefore, many uses of animation in visualization are viewed skeptically by psychologists; see the discussion by Tversky et al. [26]. For example, tasks like comparing different positions over time or identifying regions of similar behavior are difficult and time-consuming (see Fig. 1).

To overcome the issues with animated visualization, we introduce a new visualization technique for unsteady flow fields, for example, from the field of computational fluid dynamics (CFD). We describe a glyph-based approach that is able to visualize time-dependent fields with static images. The glyphs—called *flow radar glyphs*—use an intuitive mapping of the directional information that preserves certain data properties like periodicity.

Further, our glyphs can be extended to incorporate uncertainty or other cases, where a single direction per time-step is not sufficient. Like most glyph-based methods, flow radar glyphs work best in 2D. Nevertheless, the extension to 3D is covered as well. Example visualizations for data from the field of stochastic hydrogeology and CFD demonstrate the capabilities and relevance of the method. The results for the hydrogeology data were also evaluated by domain experts.

- *Marcel Hlawatsch and Daniel Weiskopf are with the Visualization Research Center (VISUS), University of Stuttgart, Germany, E-mail: {hlawatsch,weiskopf}@visus.uni-stuttgart.de.*
- *Philipp Leube and Wolfgang Nowak are with the Institut of Hydraulic Engineering (LH^2), University of Stuttgart, Germany, E-mail: {philipp.leube,wolfgang.nowak}@iws.uni-stuttgart.de.*

Manuscript received 31 March 2011; accepted 1 August 2011; posted online 23 October 2011; mailed on 14 October 2011.
For information on obtaining reprints of this article, please send email to: tvcg@computer.org.

2 Related Work

There is only little previous work in scientific visualization on static display of dynamic behavior. The main reason is that scientific visualization focuses on direct mapping of data dimensions (typically, 2D or 3D space, and time) to analogous visualization dimensions. One of the few examples of static visualization is the work by Woodring and Shen [31] on time-dependent volumetric data. This approach is generalized by Woodring et al. [32], treating 3D time-dependent data as 4D data. Joshi and Rheingans [16] also discuss methods for visualizing time-dependent data with static images, but with the focus on illustrative rendering techniques. Our approach is different from the ones mentioned above in the sense that we encode dynamic information in glyphs and allow for a dense in-place seeding of that information.

In general, glyphs have been used for a long time to visualize flow data. Using arrows to visualize flow direction is a standard method and many extensions of this basic idea are availabe, including the combination of arrow glyphs and streamlines by Bertrand and Tanguy [4] and arrow glyphs on streamsurfaces according to Löffelmann et al. [18].

Pickett and Grinstein [22] introduced with their stick-figures a more complex glyph than just simple arrows for multidimensional data. As with our approach, a dense seeding of their glyphs reveals patterns in the visualized data. De Leeuw and Van Wijk [10] also describe glyphs with higher complexity for flow visualization. Ward [27] discusses glyph placement for multivariate data and dense seeding to visualize spatial relationships. Dovey [11] shows that jittering the seeding positions by a small offset can avoid visual patterns induced by seeding on regular grids. Highlighting certain glyphs can help reduce visual overload as in the work by Boring and Pang [5]. Klassen and Harrington [17] describe how shadows can improve perception of glyphs for 3D flow. Schultz and Kindlmann [24] discuss the properties of their glyph to visualize higher-order tensors. Their glyph was designed to preserve certain characteristics of the underlying data (e.g., symmetries) in the visualization. Their design strategy is very generic; we apply it to design flow radar glyphs in Sect. 3.

In information visualization, radial mapping and ring-shaped glyphs are already a common tool. Bak et al. [2] use glyphs inspired by growth rings of trees to visualize sensor data in a spatiotemporal way. Spatiotemporal data is also visualized with the ringmaps by Zhao et al. [33]. Chen [9] employs ring glyphs to detect patterns in scientific literature. Carlis and Konstan [8] show that mapping data onto a spiral helps analyze periodicity in data. Similar concepts are presented by Weber et al. [28]. Tominski et al. [25] use helix-shaped glyphs to visualize spatiotemporal data. Burch and Diehl [7] use radial visualizations to display dynamical hierarchical information. These and further techniques can also be found in the overview by Draper et al. [12]. While our glyphs share the radial layout with the above techniques from information visualization, they differ in the actual mapping of data because our glyphs target flow field information.

The visualization of flow uncertainty remains an important research issue [15]. Zuk and Carpendale [34] present a theoretical analysis of different uncertainty visualizations that is not restricted to vector fields. Lodha et al. [19] discuss techniques to visualize the uncertainty arising from numerical integration methods. Wittenbrink et al. [30] describe glyph-based visualization of flow uncertainty. The way they represent directional uncertainty is similar to our concept; however, their glyphs are not able to display the temporal variation in a static image. For the specific case of bidirectional flow fields, Zuk et al. [35] present a glyph-based visualization of uncertainty. Texture-based methods are used by Botchen et al. [6] for uncertain unsteady flow; a similar approach is applied by Allendes Osorio and Brodlie [1]. Uncertainty in vector fields can also be incorporated in vector field topology as shown by Otto et al. [20]. More techniques for uncertainty visualization can be found in the survey by Pang et al. [21]. Note that none of the existing uncertainty visualization techniques is able to display unsteady flow in static images.

3 Flow Radar Glyphs

The basic concept of flow radar glyphs is the radial mapping of temporal variations in vector directions (see Fig. 2). Using a polar coordinate system whose center coincides with the center of the glyph vector direction is mapped to the angle and time is mapped to the radius. A temporal sequence of directions results in a spatially, radially organized sequence of points in the coordinate system. These sample points are connected according to the interpolation scheme employed for the data set. Linear interpolation results in the curve shown in Fig. 2. Hence, the directions are encoded in the positions on the curve relative to the center of the glyph. To obtain the directions from the glyph, lines can be mentally drawn from the positions on the curve to the center. This kind of mapping preserves the intuitive human notion of directions, as it is also the case with hedgehog or arrow glyphs. Fig. 3(a) illustrates how to read and interpret flow radar glyphs and Fig. 3(b) shows an example of visualization with them for a simple analytic vector field.

Further advantageous properties result from the used radial mapping. The periodicity of angles is preserved, i.e., there is no discontinuity in the visualization of angular ranges larger than 2π. This is, e.g., not the case for Cartesian plots. Symmetries in the directions are also preserved, facilitating the comparison of neighboring positions. This allows the visual analysis of data on multiple scales (Sect. 3.3). Mapping time to the radius is also beneficial: time has monotonic behavior and is constant over space, which results in constant size for all glyphs. An additional aspect of our glyph is that it converges to the classical arrow glyph as the time range covered converges to zero (Sect. 3.2) or in the case of steady flow. The local flow direction is constant in these cases, resulting in a flow radar glyph with a single line. Hence, the common vector arrows are included as a special case in flow radar glyphs. As with arrow glyphs, it is possible to mentally reconstruct streamlines by connecting these lines in these cases. This is, however, not possible in unsteady flow with the glyph covering a non-zero time range.

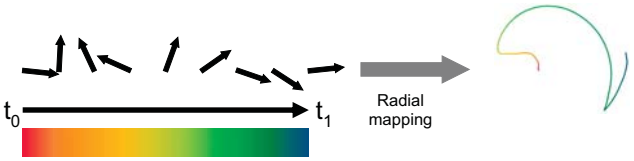

Fig. 2. Basic principle of flow radar glyphs. Direction is mapped to the angle and time to the radius of a polar coordinate system. The left sequence of directions results in the right glyph. Color mapping enhances the visualization of the temporal behavior. The above color map is used for all figures in this paper.

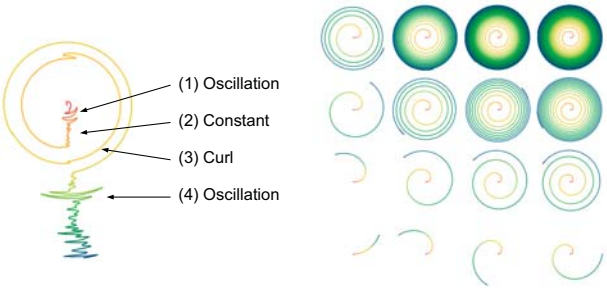

Fig. 3. (a) How to read flow radar glyphs. (1) The flow starts with a short oscillation phase in downward direction, (2) followed by almost constant downward motion. (3) A curl with two cycles follows. (4) At the end of the time range, the flow direction is again downwards with oscillations of varying intensity. (b) Visualization example of the flow (v_x, v_y) with $v_x = \cos(t^y \cdot x)$, $v_y = \sin(t^y \cdot x)$ and $0.0 \le t \le 2\pi$, $0.1 \le x \le 1.0$, and $1.0 \le y \le 3.0$. The number of periods increases in x-direction and the acceleration of the rotation increases in y-direction.

The mapping of local vector directions is intuitive because of the direct relationship to the glyph's position. Therefore, examples only of this case are presented in this paper. However, the presented concepts are not restricted to this and mappings of other directional information, such as the tangential direction along path lines, are possible.

3.1 Magnitude-Scaled Glyphs

The mapping described above has the issue that the vector magnitude is ignored. This leads to an overestimation of areas with low magnitudes. We therefore define a more general mapping to the glyph radius. Identifying the radius with path length leads to the following ordinary differential equation:

$$\frac{dr(t)}{dt} = \frac{|\mathbf{v}(t,x_0)|}{v_{\text{norm}} T}, \quad r(t_0) = 0, \tag{1}$$

where $r(t)$ is the radius at time t, $|\mathbf{v}(t,x_0)|$ is the magnitude of the vector at position x_0 and time t, v_{norm} is a normalization factor to con-

(a) (b)

Fig. 4. Comparison of magnitude-scaled and normalized flow radar glyph. (a) The magnitude-scaled glyph depicts directional variation over time, including flow magnitude. (b) The normalized glyph ignores the magnitude and shows only the directional variation. The difference is visible around the center of the glyphs. Because of low velocities at the beginning, the curl disappears in the magnitude-scaled glyph.

(a) (b) (c) (d)

Fig. 5. Different mappings of time for the same spatial position. (a) The full time range is mapped to increasing radius. (b) A smaller time range (marked in (a)) is mapped to increasing radius. (c) The color map is adapted to the selected time range from (b). (d) The full time range is mapped to decreasing radius.

trol the glyph size, and T is the time range covered by the glyph. The following equation provides then a first-order approximation of Eq. 1:

$$r_i = \frac{|\mathbf{v}_i|\,\Delta t}{v_{\text{norm}} T} + r_{i-1}.$$

Here, r_i is the radius after the i-th iteration, $|\mathbf{v}_i|$ is the magnitude of the local vector, and Δt the time range of an iteration step.

In this form, the radius is not only increased with time, but also in dependency of the vector magnitude. Hence, positions with higher average magnitude exhibit glyphs of bigger size. The drawback of this mapping is the ambiguity of the radius because different combinations of vector magnitudes over time can lead to the same radial position. This is compensated with color mapping of the temporal range.

A glyph for which the magnitude is discarded can be derived from the magnitude-scaled glyph by using normalized vectors. This leads to $r_i = \Delta t/T + r_{i-1} = i\Delta t/T$. We call this variant normalized glyph in the remainder of this paper. Fig. 4 shows a comparison of the magnitude-scaled and the normalized glyph. The visual difference between both types for a full data set can be seen in Fig. 12(a) and Fig. 12(b).

3.2 Time Range

An issue of mapping time to radius is the uneven angular resolution, which increases with increasing radius. Thus, the visual accuracy of the displayed directions is not constant over the time range. The mapping of time to increasing radius therefore emphasizes the behavior at the end of the time range (Fig. 5(a)). This is compatible with the common view that more recent events are of greater interest or importance.

But the information at the end of a temporal range in data sets is not always the most significant one. To account for this, the time range covered by the glyphs can be adapted. This helps analyze the flow behavior in more detail (Fig. 5(b)). Keeping the color map invariant when changing the time range has a similar visual effect as zooming-in on the glyph. This can be advantageous when comparing glyphs for different time ranges. But the color map can also be adapted to the selected time range such that the full color range remains available (Fig. 5(c)). This supports the interpretation of the glyphs for smaller time ranges, and helps when comparing neighboring glyphs in detail or when detecting patterns in coarse-scale visualizations (see Sect. 3.3).

However, the problem of low angular resolution at the beginning of the time range still remains. Therefore, it is also possible to invert the mapping of time to radius. In this case, time is mapped to decreasing radius and the beginning of the time range (Fig. 5(d)) is emphasized. Analyzing the data with both mappings prevents the user from missing important details at the beginning of the time range. It is also possible to use a non-linear mapping of time to emphasize certain sections of the time range. However, we recommend that the user starts the analysis with a linear mapping of time to increasing radius, which is more natural than an inverted or non-linear mapping.

All of these concepts can be applied in an interactive way by exploiting the capacity of modern GPUs (see Sect. 6).

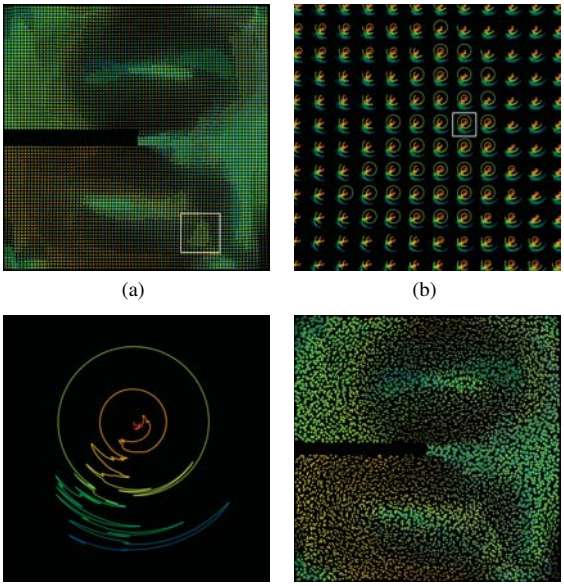

(a) (b) (c) (d)

Fig. 6. Multi-scale visualization with flow radar glyphs. (a) On the coarsest scale, patterns in the data are visible and different regions of similar behavior can be discriminated. (b) On the middle scale, neighboring positions and glyphs are comparable and the spatiotemporal behavior becomes visible in more detail. (c) On the finest scale, the temporal progression of the flow direction at individual positions can be analyzed. (d) Jittered seeding can remove patterns induced by regular seeding.

3.3 Multi-Scale Visualization

The visualization of flow data with densely seeded flow radar glyphs allows an analysis of the data on multiple scales. We identified three qualitatively different scales for the resulting visualization (Fig. 6). On the coarsest scale, many small-sized glyphs visualize a large region of the data and a partition of the data into coherent regions is visible through visual fusion (Fig. 6(a)). On the medium scale, fewer glyphs are visible with larger extent, allowing direct comparison of neighboring positions (Fig. 6(b)). The finest scale shows the zoomed-in view of single glyphs (Fig. 6(c)). This enables a detailed analysis of the temporal evolution of the flow direction. In the case of dense seeding, visual patterns can occur due to regular seeding. Jittering the seeding positions randomly by a small offset can remove these patterns. However, detecting the edges of coherent regions can also be more difficult with jittered seeding (Fig. 6(a) and Fig. 6(d)). Further examples of multi-scale visualization are presented in the result section (Sect. 7).

We suggest the following work flow for the visual analysis with flow radar glyphs: The user starts with a zoomed-out view to detect interesting areas and patterns in the data. Switching between regular and jittered seeding can help classify the occurring patterns. They can then analyze the spatiotemporal behavior in these areas in more detail by zooming-in. If interested in the detailed temporal evolution of the flow direction, e.g., to observe the effects of certain events on it, they can examine single glyphs. Changing the time range (Sect. 3.2) can further help understand temporal processes in the flow.

(a) (b) (c)

Fig. 7. Comparison to path and streak lines. (a) Regularly seeded path lines with a tenth of the full time range used as integration range. (b) Regularly seeded streak lines with half of the integration range of (a). (c) Magnitude-scaled flow radar glyphs covering the full time range.

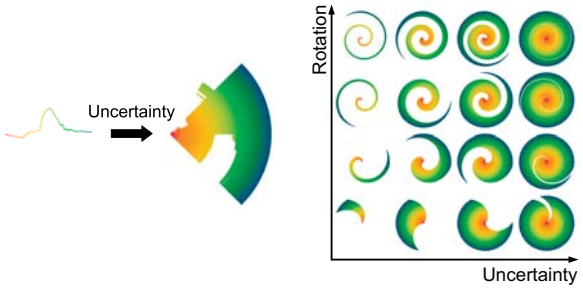

(a) (b)

Fig. 8. (a) Extension of the glyph to uncertain directions. Without uncertainty, a single curve represents the directional variation over time. In the case of uncertain directions, their angular range is represented by an arc instead of a single point. These arcs form a filled area that represents the temporal evolution of the angular range. (b) Problems of the glyph when visualizing strong rotation and high uncertainty. In this matrix, the uncertainty increases in *x*-direction and the strength of rotation in *y*-direction.

3.4 Comparison to Existing Techniques

Common state-of-the-art methods for the visualization of unsteady flow are animated arrow glyphs and the representation by path or streak lines (as geometrically rendered lines or indirectly in the form of texture-based flow visualization). Arrow glyphs show directions in a single time step, and only animating them allows the analysis of temporal processes. If only a static image is available, it is also possible to display a sequence of arrow glyphs (see Fig. 1). In both cases, the analysis and comparison of multiple spatiotemporal positions are difficult. Fig. 1 shows that the differences of the neighboring positions can easily be detected with flow radar glyphs. The same information can be gained with arrow glyphs, but more effort is required to compare neighboring positions. Even when analyzing only a single position, small temporal details can be missed, like the small oscillation in the upper row before the direction turns downward and back to the right.

Flow radar glyphs cannot directly be compared with path or streak lines because the latter visualize Lagrangian properties. However, they are common tools for analyzing unsteady flow, and a qualitative comparison can be done (Fig. 7). The figure shows that it is quite difficult to analyze the full spatiotemporal domain of the field due to the susceptibility to visual clutter of these methods. Even with the recently published method by Weinkauf et al. [29], which reduces clutter for characteristic curves, the visual signature of flow radar glyphs fundamentally differs from line-based methods.

Another problem is that path or streak lines depend on seeding in space and time. Therefore, they are typically used in animated visualization—with the problems of cognitive load inherent to animated visualizations. In contrast, flow radar glyphs can display the full temporal range of the data without visual clutter. And as a further advantage, the glyphs can incorporate uncertainty with all spatiotemporal details (see Sect. 4).

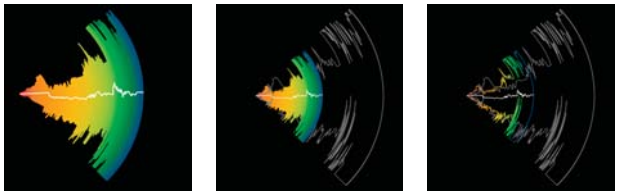

(a) (b) (c)

Fig. 9. Different types of flow radar glyphs for uncertainty. (a) This variant visualizes the range of directions as filled area. The average direction is displayed as white curve. (b) Overlaid on the glyph from (a), additional contours show the range for the minimum and maximum magnitude (both gray). (c) This variant shows the same information as (b) but uses contours only.

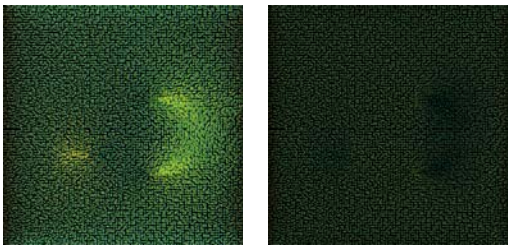

(a) (b)

Fig. 10. Attenuation of uncertain positions. (a) Directly drawing the glyphs emphasizes positions with high uncertainty due to the larger extent of the glyphs there. (b) Modulating transparency with uncertainty attenuates these positions and emphasizes regions with low uncertainty.

4 Visualizing Uncertainty

The extension of flow radar glyphs to uncertain flow fields or other data for which a range of directions is defined (instead of a unique vector per point in space and time) is quite straightforward. To cover these cases, we apply the concept of the glyph to the two limiting angles (or statistical percentiles) of the angular range of directions. The two resulting curves represent the contour of the glyph in the uncertain case. The area in between can be filled to visually represent the angular ranges (Fig. 8(a)). Instead of single points representing single directions at given positions in space and time, an arc displays the possible range of directions. An issue of this approach is that the glyph is difficult to read in cases of strong rotation and high uncertainty (Fig. 8(b)). Nevertheless, a qualitative comparison with other positions is still possible, but a quantitative analysis is more difficult.

The glyph can be further extended to visualize more aspects of uncertain vector fields (Fig. 9). For example, the statistically averaged direction can be visualized with an additional curve (Fig. 9(a)). If vector magnitude is uncertain and of interest, the glyph can be extended to additionally show the contours of the glyphs with lowest and highest magnitudes (Fig. 9(b)). The contours provide an impression of the possible ranges of directions and magnitudes. To reduce visual clutter, this variant can be displayed without the filled area of the glyph that represents the average magnitude (Fig. 9(c)).

Filling the glyph to visualize the directional range without further modifications has the effect that positions with high uncertainty appear brighter in large-scale views because they cover a larger amount of pixels of the image (Fig. 10(a)). This is beneficial when areas with high uncertainty are of primary interest. Often, however, areas of low uncertainty should be emphasized more. To achieve this, the transparency of the glyphs can be modulated according to the degree of uncertainty (Fig. 10(b)): positions with high uncertainty are assigned high transparency and fade out.

We suggest to use the filled type without contours (Fig. 8), possibly with the averaged direction overlaid (Fig. 9(a)), for large-scale analy-

(a) (b) (c) (d) (e)

Fig. 11. Extension of the glyph to 3D. (a) A 3D version of the glyph is defined by mapping direction to the two angles of spherical coordinates and time to the radius. (b) Close-up of a single 3D glyph (marked in (a)). The glyph is hard to interpret without lighting. (c) Improved depth perception with a simple shading scheme—the normal component relative to the seeding plane controls the shading intensity. (d) The same glyph now viewed along the normal direction of the plane. (e) The glyph projected onto the plane. The shading still allows perception of the normal component.

sis. The glyphs extended with the minimum and maximum magnitude should only be used on smaller scales to avoid visual clutter. The use of uncertainty modulated transparency strongly depends on the application. Hence, it is best to let the user interactively switch between both options to provide an impression of the uncertainty in the data.

5 Three-Dimensional Flow

In this section, we sketch an extension of our glyph for 3D data. The visualization of 3D data is challenging because of occlusion and projection issues, which are inherent to any 3D flow visualization method. We focus on regular seeding on a plane through the data. Other seeding strategies on planar or non-planar 2D manifolds through 3D space should be feasible without changes to the glyphs. The extension to seeding at arbitrary 3D positions would be more challenging because of issues of occlusion and the lighting model that we use (see below). It is important to note that the glyphs, even if seeded on 2D manifolds, are designed to show the full 3D vectors at the sample positions.

Instead of polar coordinates, we use now spherical coordinates for the glyphs. The direction is mapped to the two angles ϕ and θ, and the time is mapped to the radius (Fig 11(a)). Usually, depth perception can be improved by appropriate lighting. We employ a simplified shading model that only takes the flow's normal component relative to the seeding plane (or tangent plane of the 2D manifold) into account (Fig 11(c)). This shading model allows us to keep the nice characteristics of visual fusion for zoomed-out images, similar to the 2D case. In this way, we can recognize temporal and spatial patterns in the flow. For best perception of the tangential flow components, the viewing direction should be close to the direction of the normal of the seeding plane (Fig 11(d)). However, there is still the problem of distortions and overlap with neighboring glyphs through to the projection of 3D geometry, especially if the viewing direction is far from the normal of the plane. This affects the perception of patterns in the data. To address this issue, we project the glyphs onto the seeding plane by neglecting the flow's normal component for the geometry of the glyphs (Fig 11(e)). The normal component is now only used for the shading, controlling a factor for adding white color to the color of the glyphs. The result is that glyphs with normal components antiparallel to the viewing direction are lighter, and normal components parallel to the viewing direction make the glyphs darker.

This 3D version of flow radar glyphs visualizes the directional component of the flow in the plane by geometry and the component normal to the plane through shading. The capabilities of the glyph are retained: patterns are visible on zoomed-out images and close-ups allow a detailed analysis of 3D flow directions (see Sect. 7.3).

The 3D flow radar glyph discussed here is meant as a proof-of-concept showing that it is possible to extend the concept of flow radar glyphs to 3D flow. There is still potential for improvements of the 3D glyph. Many well-known techniques for visualizing 3D lines and geometry could be applied, e.g., advanced shading models, shadows, or depth of field. Adequate interaction concepts and the use of stereo displays could further improve the perception of single glyphs. Such extensions of the 3D glyph are subject of future work.

6 Implementation

Our visualization approach was implemented with OpenGL, GLSL, and CUDA for nVidia GPUs. The basic implementation of our method is straightforward: it is sufficient to draw the described curves (Sect. 3) for every glyph. Since the glyphs allow a static visualization, their geometry can be pre-computed and only the rendering of the geometry has to be fast enough to allow interactive navigation (zooming etc.). However, it is beneficial if the user can interactively change certain parameters of the glyphs, like their size or the time range covered by them. In this case, the shape of the glyph has to be re-computed fast enough for interactivity, which is more challenging.

We implemented two approaches for this: a geometry-based approach and an image-space approach. The geometry-based approach renders a geometric curve for every glyph. This allows high visual accuracy even when strongly zooming-in on individual glyphs. To generate the geometry fast enough for interactive updates of the glyph, CUDA is used to compute the vertices of the glyphs in parallel on the GPU and to write them into an OpenGL Vertex Buffer Object (VBO). OpenGL can directly render the geometry in the VBO without additional memory transfer. If the number of glyphs is not too large, this is fast enough to change parameters interactively. However, GPU memory consumption is high, in particular for a large number of glyphs or if the glyphs cover a wide time range. Adapting the complexity of the geometry to the size of the glyphs could reduce this problem. Beside high accuracy, other advantages of this approach are the easy handling of non-regular seeding schemes and overlapping glyphs.

The image-space approach is similar to local GPU ray casting, a successful generic strategy in computer graphics; see, for example, ellipsoid ray casting by Gumhold [13]. Bounding geometry is rendered and fragment shader programs are executed for the covered pixels. Inside the shader program, it is checked if the current pixel is part of the glyph. This is done by computing the temporal and directional range covered by the pixel and comparing it to the corresponding range in the data. If these ranges overlap, the pixel is drawn. The limitation of this method is the reduced accuracy because the exact computation of the range covered by a single pixel is complex. Additionally, variants of the glyph and of the glyph rendering are quite complex to implement, e.g., rendering magnitude-scaled glyphs or overlapping glyphs. However, there are several advantages of this solution. The rendering time depends only on the output resolution; a huge number of glyphs can still be rendered interactively. Since the glyphs are computed on-the-fly, all parameters of the glyph, like the time range covered, remain interactively changeable. Furthermore, the extension to uncertainty requires only checking a different angular range in the shader.

7 Results

To demonstrate the capabilities of flow radar glyphs, examples of three different types of data are presented in this section. The first example visualizes 2D data from a turbulent CFD simulation of air in a closed room subject to heating. It demonstrates how to visually compare different simulation runs for parameter studies. The second example, taken from the field of environmental engineering, is a 2D simulation

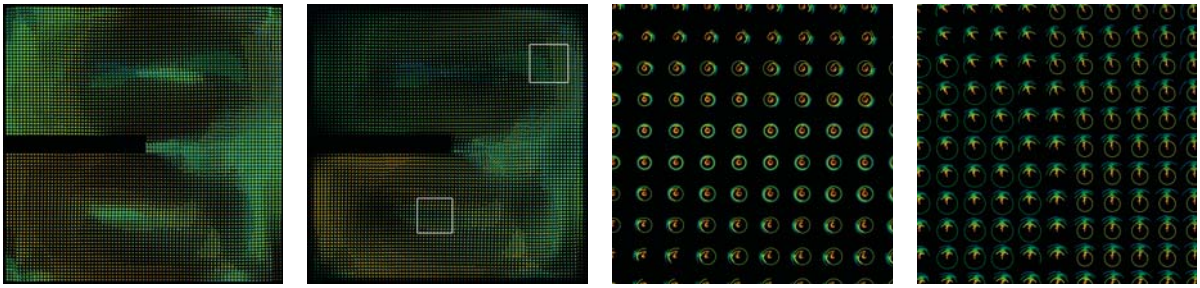

(a) (b) (c) (d)

Fig. 12. Visualization of the 2D CFD data for the single setup. (a) Overview with normalized glyphs. (b) Overview with magnitude-scaled glyphs. (c) Close-up on the center of the lower whirl. (d) Close-up on the region in the top right corner. The close-up regions are marked in (b).

of groundwater flow and the influence of three wells in a remediation setup for contaminated aquifers. This example shows how the glyphs can visualize the uncertainty quantified by stochastic or statistical simulations. The last example is a 3D CFD simulation of an overflowed cuboid that illustrates the extension of the glyphs to 3D.

7.1 Two-Dimensional CFD Data and Parameter Studies

The CFD data result from a 2D finite volume simulation of air in a closed room. The bottom is heated and the top cooled, both with constant temperature. The room is partially divided by a rectangular barrier in the middle of the room. The data sets have a uniform grid with a spatial resolution of 41×41 and 320 time steps.

7.1.1 Single-Parameter Setup

In this setup, the temperature boundary condition was 250 °C on the bottom and 5 °C on the top. Fig. 12(a) shows an overview of the data set with normalized flow radar glyphs. Large areas of different behavior are visible. Whirls with moving centers are below and above the barrier. Another area grows from the barrier to the right with extensive directional variations. The magnitude-scaled glyphs (Fig. 12(b)) additionally depict the variation in flow velocity, e.g., low velocities in the center of the whirls and in the corners.

The close-ups (Fig. 12(c) and Fig. 12(d)) allow a more detailed analysis of flow behavior. Fig. 12(c) shows the center of the lower whirl. This area exhibits uniform behavior in the first half of the simulation. After that, the moving center of the whirl induces a significant change of the flow behavior above and below its path: the flow oscillates heavily with an average direction to the right (upper part of Fig. 12(c)) respectively to the left (lower part). For Fig. 12(d), a region with two smaller areas in the top right was chosen. A small, separating area between them is visible (Fig. 12(b)). Left and right from this separating area, a single curl occurs at different points in time. Apart from that, the flow behavior is almost uniform there.

7.1.2 Parameter Study

Fig. 13 shows results for three examples from the parameter study, where the temperature of the bottom was varied, while the temperature on the top was kept unchanged. Comparing the overview images (Fig. 13(a), 13(e), and 13(i)), we observe that the structures of the two high temperature results are more consistent and differ qualitatively from the low temperature result. Both high temperature cases exhibit the large areas described in Sect. 7.1.1, whereas the low temperature result exhibits less intense areas with two whirls at the bottom. In the result for the highest temperature, the area of high eddy intensity starting at the barrier extends farther and the flow in the top left corner exhibits more pronounced turbulence. We conclude that high temperature generates stronger turbulence.

In the close-up areas of the second column, the two lower temperature results exhibit similar behavior: curls followed by constant flow direction. With the highest temperature at the bottom, curls appear only at the left border at the end of the time range. In the third column, the flow for the configuration with lowest temperature exhibits less turbulent behavior than the high temperature configurations. In these two configurations, flow directions towards the barrier are visible. The last column again shows high turbulence for the two high temperature configurations. The flow of the low temperature configuration has only little turbulence there, similar to the region in Fig. 13(b).

7.2 Groundwater Simulation with Uncertainty

In-Situ chemical oxidation (ISCO) techniques with injected clean-up reactants have proven to be powerful tools in order to clean up contaminated soils [14]. Their attraction lies in conceptual simplicity and low technological effort. However, successful application requires a profound understanding and fine-tuned control of the underlying processes, most of all concerning a closed-loop flow field between injection and extraction wells for the clean-up reactants. The generic lack of knowledge about on-site conditions requires predictive simulation and evaluation prior to the field implementation. This is a non-trivial task since the system is space- and time-dependent and subject to small-scale uncertainty of material parameters that define the permeability for groundwater flow [23].

Fig. 14 shows a typical remediation setup for in-situ oxidation. Well (A) injects the reactant into an ambient groundwater flow (from left to right). The injected reactant passes through the contaminated zone and well (B) extracts the residual reactant. The success depends, among other things, on the percentage of residual reactant that can be extracted at well (B). If the wells (A) and (B) are not perfectly aligned with the regional ambient groundwater flow, not all the reactant injected in well (A) will be captured by the extraction well (B). To avoid this, a second extraction well (C) is drilled in order to capture the reactant missed by well (B).

In this example, we consider the problem of an imperfect well setup (e.g., occurring under seasonal variations of ambient flow). In order to reveal the system response during an injection at (A) with extraction at (B) and additional pumping at (C), the simulation is evaluated through four different periods of pumping regimes (Fig. 14, right). Regions of interest are the so-called stagnation points (left of (A) and right of (B) and (C)), where the ambient flow and the individual flow components from the wells cancel out, leading to regions with very low velocities, very large residual times, and occurrence of all flow directions around each stagnation point.

The remediation problem is discretized on a 128×128 cell grid, and evaluated at 250 time steps covering all four periods (50 time steps for the first three periods, and 100 time steps for the last period). Because the investigated system is very flat compared to its other dimensions, and because the system force is typically uniform over the entire depth, depth-integrated (2D) simulations of flow are fully sufficient in this and many other cases. A Poisson-type partial differential equation based on Darcy's law is used for creeping (potential) flow in porous media [3]. The lack of prior knowledge about on-site conditions is accounted for by 500 Monte-Carlo runs of the flow equation with randomized geostatistical permeability fields [23].

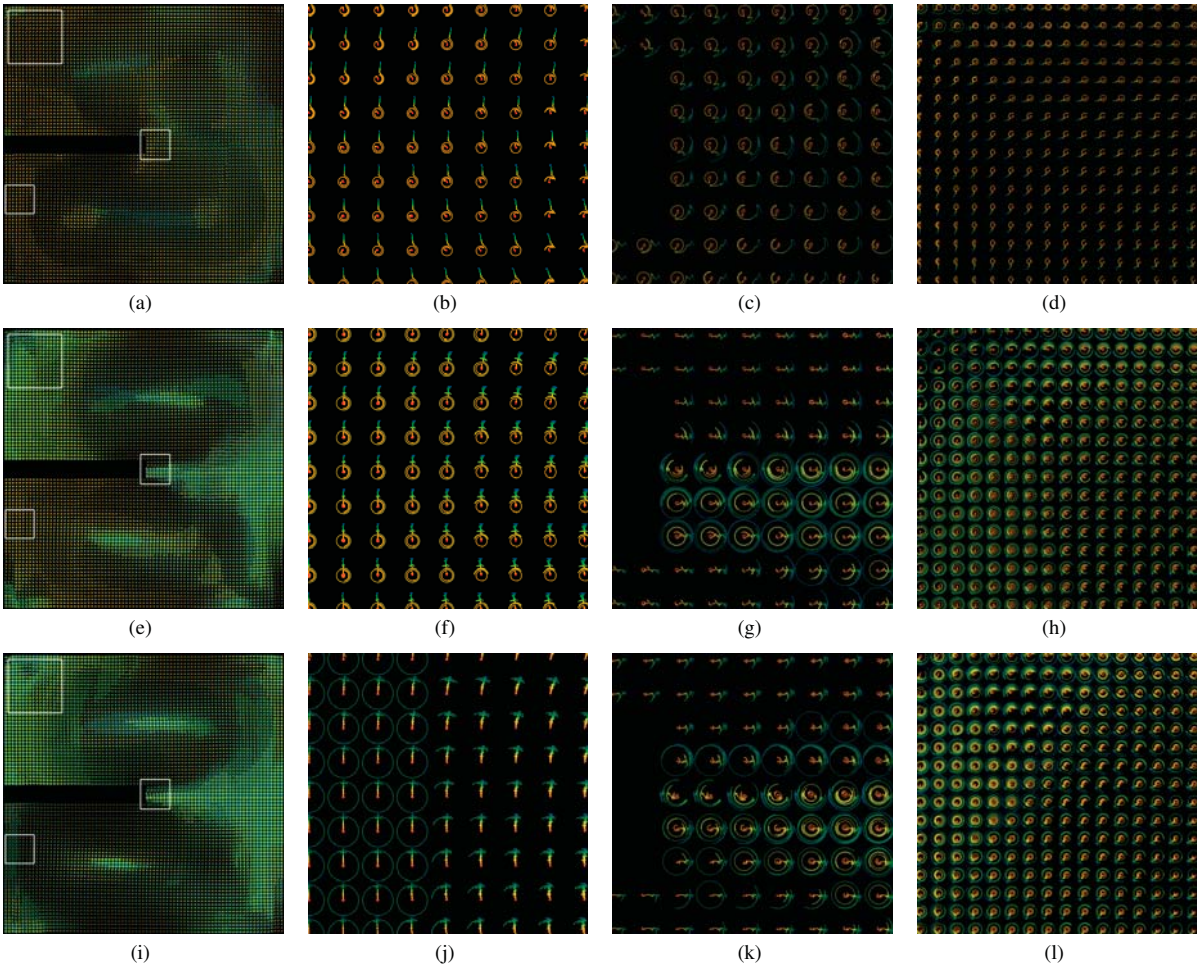

Fig. 13. Visualization for the parameter study with normalized glyphs. Each row belongs to one configuration of the parameter study with different temperature on the bottom: 25°C in the first row, 250°C in the second, and 500°C in the third. The temperature on the top was 5°C for all configurations. The close-ups show the same areas in each column, marked in the overview images (left column). The second column shows the lower left area, the third column the area at the barrier, and the fourth column the area in the top left corner. Visual comparison of the images of the same column allows us to analyze the influence of the temperature on the flow.

7.2.1 Average Flow Direction

Fig. 15 shows the flow direction averaged over all Monte-Carlo runs visualized with flow radar glyphs. The influence of the wells on groundwater flow is clearly visible in the glyphs, whereas the uncertainty in permeability that affects the flow field is averaged out. Undistorted glyphs reveal regions with no well influence, whereas bent glyphs show a high sensitivity to temporal changes in pumping activity. The orientation of the bend indicates the change of average flow direction during changes in well activity. Lower velocities at the right domain boundary are visible.

7.2.2 Single Monte-Carlo Run

Results for a single Monte-Carlo run are shown in Fig. 16. The first close-up (Fig. 16(b)) shows a region above well (C). It is clearly visible that the activation of (C) causes a change in flow direction towards well (C). When injection at (A) ends, the flow turns even more towards (C). The end of pumping at (B) and (C) allows the system to recover to the original ambient flow direction (from left to right); spatial variations remain only due to the heterogeneous permeability. Fig. 16(c) focuses on the region left of well (B). Obviously, this region is almost insensitive to changes in well activity at (A) and (C). Only minor changes of the flow direction can be observed. A close-up of the region left of well (A) is shown in Fig. 16(d). Here, only positions close to the well are significantly affected by well activity. This is because the ambient flow (from left to right) and the flow from the well have opposed flow directions in this area, and the radius of influence of the well is too small to significantly affect other regions.

7.2.3 Flow Uncertainty

Finally, we demonstrate how to visualize and analyze spatiotemporal changes in uncertainty with flow radar glyphs. Uncertainty associated with direction and velocity of flow is quantified based on the 10th and 90th percentiles of all Monte-Carlo simulation runs. Fig. 17 shows the spatiotemporal distribution of uncertainty resolved for time ranges that cover the different pumping regimes (0), (2), and (3). Fig. 17(b) and 17(c) indicate that the highest uncertainty occurs close to all wells, i.e., in the regions around the possible locations of the three stagnation points (filled flow radar glyphs). Fig. 17(d) shows the component of uncertainty due to the underlying geostatistical randomness of permeability (without any well activity). Apparently, uncertainty has a homogeneous character throughout the domain, except at the left and right borders, where the imposed boundary conditions dictate a lower uncertainty. This is obvious since the Monte-Carlo ensemble is designed to represent the manifold of possible spatial patterns and, as a matter of the input statistics, the frequency of possible outcomes is uniform throughout the domain. Fig. 18 provides a more detailed analysis of the simulation result. It reveals that uncertainty decreases whenever

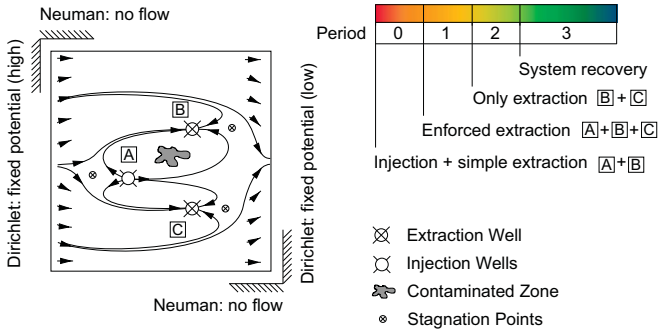

Fig. 14. Remediation setup (left) for in-situ oxidation with one injection (A) and two extraction (B, C) wells operating according to the pumping configuration (top right). The contaminated zone is located between (A) and (B). Boundaries are implemented as no-flow (northern and southern) and fixed potential (eastern and western) boundaries with regional ambient groundwater flow from left to right.

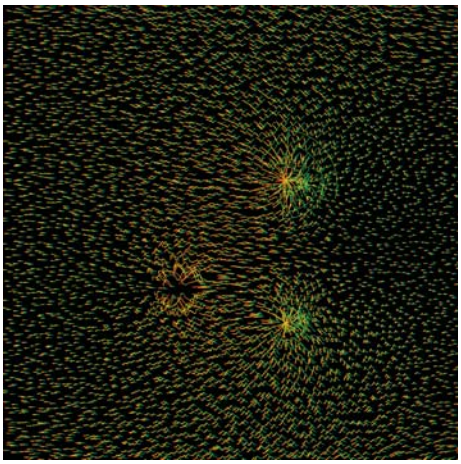

Fig. 15. Flow directions averaged over all Monte-Carlo runs. Magnitude-scaled flow radar glyphs on a jittered regular seeding grid show the temporal evolution of the flow. Accumulation of flow radar glyphs at (B, C) and separation at (A) characterize the location of the extraction respectively injection wells. Increasing velocities towards active wells result in regions of overlapping glyphs.

and wherever the flow directions induced by any of the wells coincide with the ambient flow direction of the regional background flow (Fig. 18(b) transition to period (1)). If these individual flow components are opposed to each other, e.g., close to the stagnation points, the uncertainty in flow angle is increased (Fig. 18(c) transition to period (1)). The reason for this is the physics of flow: all possible flow directions occur around the stagnation point, and the positions of the stagnation points changes in every simulation run. A similar effect can be observed between wells (B) and (C) (Fig. 18(d)).

7.2.4 Lessons Learned

From joint sessions with domain and visualization experts, we report the following experiences. The domain experts indicated that the combined visualization of spatiotemporal flow behavior and uncertainty by flow radar glyphs provided insight that would be much more time-consuming to obtain with their prior visualization techniques. They usually employ multiple plots with color mapping for different features of the data, e.g., uncertainty and average direction, but not a combined visualization. The domain experts learned how to work with the glyph visualization just within minutes, i.e., there is no steep learning curve. They saw the main application in understanding boundary conditions (even for arbitrary complex geometries), force terms that vary in space and time, and arbitrary complex input statistics. They reported that the technique could improve the analysis of complex, uncertain, dynamic, and distributed systems. Beside scientific purposes, they suggested the glyph visualization as a powerful didactical tool in education. Their main criticism was that details of the temporal evolution get lost on the overview level.

7.3 Three-Dimensional CFD Data

The data set (uniform grid with spatial resolution $121 \times 51 \times 101$ and 70 time steps) results from a 3D CFD simulation of the turbulent flow over a cuboid. The cuboid on the left side (Fig. 19) is overflowed from left to right. Behind the cuboid, a Kármán vortex street appears.

The glyphs in Fig. 19(a) depict the oscillation of the flow direction in the Kármán street. The region, where the flow is not affected by the cuboid, can be identified. The shading of the glyphs (Sect. 5) in the close-up (Fig. 19(b)) reveals the huge normal component in this area with oscillating directions in the x/z-plane. In Fig. 19(c), the Kármán street causes visible patterns right of the cuboid. The dark shading of the glyphs near the cuboid indicate normal components parallel to the viewing direction. The downward direction of the flow behind the cuboid (see Fig. 19(a)) is the reason for this. The oscillating directions in the x/z-plane are visible in detail in Fig. 19(d).

8 Conclusion and Future Work

The strength of the presented glyphs is their ability to visualize time-dependent processes in a static way. Further, the extension to data without unique directions, e.g., data with uncertainty, is straightforward and intuitive. The design of the glyph preserves angular periodicity and directional symmetries. The presented examples show that the glyphs allow a multi-scale visualization of flow data and how they support the analysis of time-dependent processes and phenomena. Results from different simulation runs, e.g., within parameter studies, can be compared in detail. In the case of uncertainty, the glyphs show not only the distribution of uncertainty, but also directional information and its temporal behavior. Among static visualization, the latter is an unprecedented capability.

In contrast to path or streak lines, the glyphs can always be scaled appropriately to avoid visual clutter. In many cases, it is easier, faster and more insightful to analyze time-dependent data with flow radar glyphs than with animated arrow glyphs. Even in cases where the animated approach might perform better, an implementation of flow radar glyphs can be used because they converge against arrow glyphs at the limit of infinitesimally small time ranges. Although there is potential to improve the 3D version of the glyph, it is clear that flow radar glyphs work best for 2D data. The scenario and results for the stochastic 2D groundwater simulation show that there are still many relevant 2D applications that can benefit from our method.

A further advantage of our method is its suitability for parallelization, as there exists no dependency between individual glyphs. Because every glyph covers only a single point in space, it is trivial to sub-divide and distribute the underlying data, e.g., for cluster computation and visualization on large high-resolution displays.

The focus of this paper is to visualize the temporal evolution of local vector directions. Future work could include the application of the presented glyphs to non-local properties, e.g., to the tangential direction along path lines. Further, it might be possible to apply flow radar glyphs to symmetric second-order tensor fields, e.g., stress tensor fields, where multiple directions are defined at a single position. The 3D variant of the glyph could be improved, e.g., via shadows or other shading models that help improve depth perception. Finally, a quantitative user study could be conducted to assess strengths and weaknesses of the method in more detail.

Acknowledgments

The authors would like to thank the German Research Foundation (DFG) for financial support of the project within the *Cluster of Excellence in Simulation Technology* (EXC 310/1) at Universität Stuttgart. The authors would also like to thank Filip Sadlo for fruitful discussion and help with the CFD data.

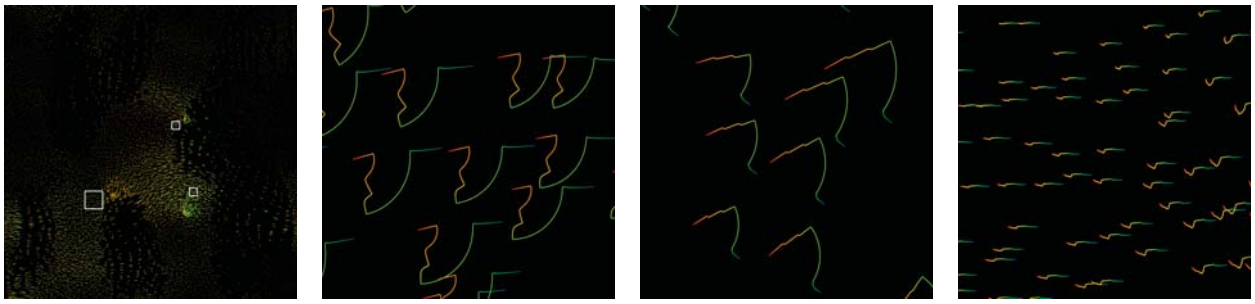

(a) (b) (c) (d)

Fig. 16. Results for a single Monte-Carlo run. (a) Overview with magnitude-scaled glyphs on a jittered regular seeding grid. Close-up areas (marked in (a)) include: (b) above well (C), (c) left from well (B), and (d) left from well (A). See Fig. 14 for well denotations.

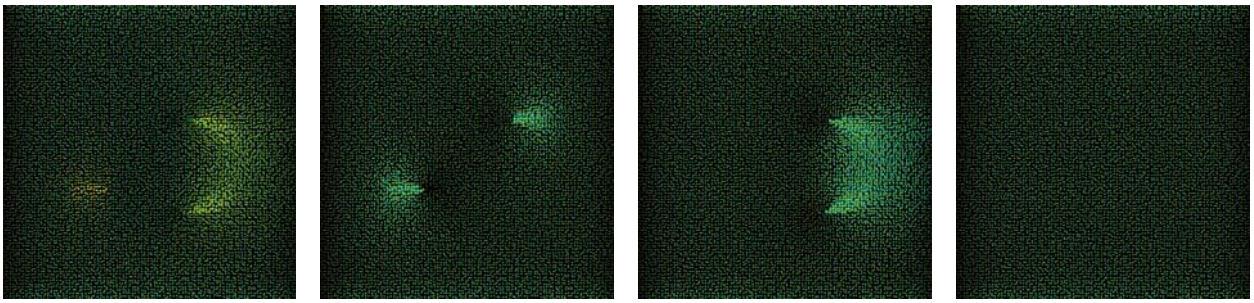

(a) (b) (c) (d)

Fig. 17. Uncertainty of flow direction based on the 10th and 90th percentiles of all Monte-Carlo runs. Normalized glyphs are seeded on a regular grid. In order to highlight uncertainty, no transparency modulation (see Sect. 4) is used. Note that the color map is adapted to the selected time ranges (see Sect. 3.2). (a) visualizes the full time range whereas (b) focuses on period (0). (c) shows period (2), and period (3) is depicted in (d).

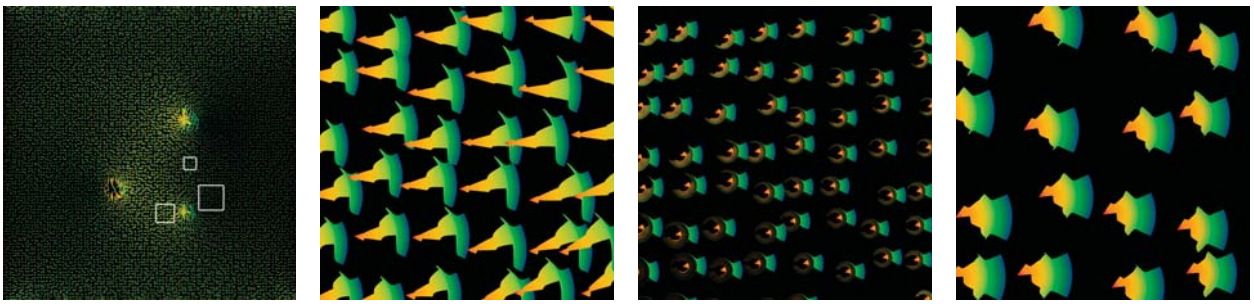

(a) (b) (c) (d)

Fig. 18. Detailed analysis of flow uncertainty. The magnitude-scaled glyphs are seeded on a jittered regular grid, transparency modulation (see Sect. 4) is used. (a) Overview with close-up areas marked. (b) Close-up of the area left to well (C). (c) Close-up of the area right of well (C). (d) Close-up of the area below well (B). See Fig. 14 for well denotations.

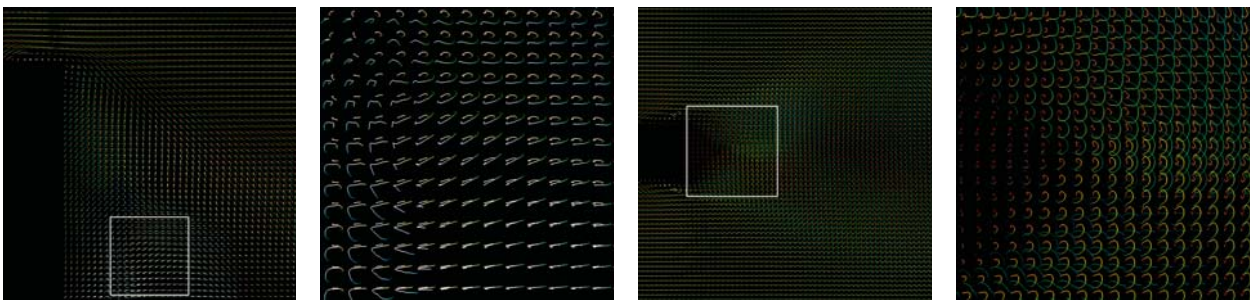

(a) (b) (c) (d)

Fig. 19. Visualization of the 3D CFD data with magnitude-scaled 3D flow radar glyphs regularly seeded on a plane. (a) Zoomed-out image of glyphs seeded on a plane in x/y-direction. (b) Close-up of the region marked in (a). (c) Zoomed-out image of glyphs seeded on a plane in x/z-direction. (d) Close-up of the region marked in (c).

REFERENCES

[1] R. S. Allendes Osorio and K. W. Brodlie. Uncertain flow visualization using LIC. In *Proceedings of EG UK Theory and Practice of Computer Graphics*, pages 1–9, 2009.

[2] P. Bak, F. Mansmann, H. Janetzko, and D. Keim. Spatiotemporal analysis of sensor logs using growth ring maps. *IEEE Transactions on Visualization and Computer Graphics*, 15(6):913–920, 2009.

[3] J. Bear. *Dynamics of Fluids in Porous Media*. Elsevier, 1972.

[4] F. H. Bertrand and P. A. Tanguy. Graphical representation of two-dimensional fluid flow by stream vectors. *Communications in Applied Numerical Methods*, 4(2):213–217, 1988.

[5] E. Boring and A. Pang. Directional flow visualization of vector fields. In *Proceedings of IEEE Visualization 1996*, pages 389–392, 1996.

[6] R. Botchen, D. Weiskopf, and T. Ertl. Texture-based visualization of uncertainty in flow fields. In *Proceedings of IEEE Visualization 2005*, pages 647–654, 2005.

[7] M. Burch and S. Diehl. TimeRadarTrees: Visualizing dynamic compound digraphs. *Computer Graphics Forum*, 27(3):823–830, 2008.

[8] J. V. Carlis and J. A. Konstan. Interactive visualization of serial periodic data. In *Proceedings of UIST 1998*, pages 29–38, 1998.

[9] C. Chen. Citespace II: Detecting and visualizing emerging trends and transient patterns in scientific literature. *Journal of the American Society for Information Science and Technology*, 57(3):359–377, 2006.

[10] W. C. de Leeuw and J. J. van Wijk. A probe for local flow field visualization. In *Proceedings of IEEE Visualization 1993*, pages 39–45, 1993.

[11] D. Dovey. Vector plots for irregular grids. In *Proceedings of IEEE Visualization 1995*, pages 248–253, 1995.

[12] G. Draper, Y. Livnat, and R. Riesenfeld. A survey of radial methods for information visualization. *IEEE Transactions on Visualization and Computer Graphics*, 15(5):759–776, 2009.

[13] S. Gumhold. Splatting illuminated ellipsoids with depth correction. In *Proceedings of VMV 2003*, pages 245–252, 2003.

[14] S. Huling and B. Pivetz. In-Situ Chemical Oxidation. Technical report, EPA 600-R-06-072. US Environmental Protection Agency (USEPA), 2006.

[15] C. Johnson. Top scientific visualization research problems. *IEEE Computer Graphics and Applications*, 24(4):13–17, 2004.

[16] A. Joshi and P. Rheingans. Illustration-inspired techniques for visualizing time-varying data. In *Proceedings of IEEE Visualization 2005*, pages 679–686, 2005.

[17] R. V. Klassen and S. J. Harrington. Shadowed hedgehogs: A technique for visualizing 2D slices of 3D vector fields. In *Proceedings of IEEE Visualization 1991*, pages 148–153, 1991.

[18] H. Löffelmann, L. Mroz, and E. Gröller. Hierarchical streamarrows for the visualization of dynamical systems. In *Proceedings of the 8th EUROGRAPHICS Workshop on Visualization in Scientific Computing*, pages 203–211, 1997.

[19] S. K. Lodha, A. Pang, R. E. Sheehan, and C. M. Wittenbrink. UFLOW: Visualizing uncertainty in fluid flow. In *Proceedings of IEEE Visualization 1996*, pages 249–254, 1996.

[20] M. Otto, T. Germer, H.-C. Hege, and H. Theisel. Uncertain 2D vector field topology. *Computer Graphics Forum*, 29(2):347–356, 2010.

[21] A. T. Pang, C. M. Wittenbrink, and S. K. Lodha. Approaches to uncertainty visualization. *The Visual Computer*, 13(8):370–390, 1997.

[22] R. Pickett and G. Grinstein. Iconographic displays for visualizing multidimensional data. In *Proceedings of the IEEE International Conference on Systems, Man, and Cybernetics 1988*, pages 514–519, 1988.

[23] Y. Rubin. *Applied Stochastic Hydrogeology*. Oxford University Press, 2003.

[24] T. Schultz and G. Kindlmann. A maximum enhancing higher-order tensor glyph. *Computer Graphics Forum*, 29(3):1143–1152, 2010.

[25] C. Tominski, P. Schulze-Wollgast, and H. Schumann. 3D information visualization for time dependent data on maps. In *Proceedings of the Ninth International Conference on Information Visualisation*, pages 175–181, 2005.

[26] B. Tversky, J. B. Morrison, and M. Betrancourt. Animation: can it facilitate? *International Journal of Human-Computer Studies*, 57(4):247–262, 2002.

[27] M. O. Ward. A taxonomy of glyph placement strategies for multidimensional data visualization. *Information Visualization*, 1(3-4):194–210, December 2002.

[28] M. Weber, M. Alexa, and W. Müller. Visualizing time-series on spirals. In *Proceedings of IEEE Symposium on Information Visualization 2001*, pages 7–13, 2001.

[29] T. Weinkauf, H. Theisel, and O. Sorkine. Cusps of characteristic curves and intersection-aware visualization of path and streak lines. In *Proceedings of TopoInVis*, 2011.

[30] C. Wittenbrink, A. Pang, and S. Lodha. Glyphs for visualizing uncertainty in vector fields. *IEEE Transactions on Visualization and Computer Graphics*, 2(3):266–279, 1996.

[31] J. Woodring and H.-W. Shen. Chronovolumes: a direct rendering technique for visualizing time-varying data. In *Proceedings of the 2003 Eurographics/IEEE TVCG Workshop on Volume graphics*, pages 27–34, 2003.

[32] J. Woodring, C. Wang, and H.-W. Shen. High dimensional direct rendering of time-varying volumetric data. In *Proceedings of IEEE Visualization 2003*, pages 417–424, 2003.

[33] J. Zhao, P. Forer, and A. S. Harvey. Activities, ringmaps and geovisualization of large human movement fields. *Information Visualization*, 7:198–209, June 2008.

[34] T. Zuk and S. Carpendale. Theoretical analysis of uncertainty visualizations. In *Proceedings of SPIE-IS&T Conference on Electronic Imaging*, pages 66–79, 2006.

[35] T. Zuk, J. Downton, D. Gray, S. Carpendale, and J. Liang. Exploration of uncertainty in bidirectional vector fields. In *Proceedings of SPIE-IS&T Conference on Electronic Imaging*, 2008.